AIAA SciTech Forum
January 3-7, 2022, San Diego, CA & Virtual
AIAA SCITECH 2022 Forum

10.2514/6.2022-2400

CFD-Assisted Calibration of a Multi-Hole Probe for a Small UAS

Robert Sasse*, Steve Borenstein†, Radiance Calmer‡, Michael Rhodes§, John Farnsworth¶,Gijs de Boer‖**††‡‡, and Brian M. Argrow§§
University of Colorado, Boulder, CO, 80309, USA

John J. Bird¶¶
The University of Texas at El Paso, El Paso, TX, 79968

A method for calibrating a multi-hole probe (MHP) used for inertial wind vector measurements from a small Uncrewed Aircraft System (sUAS) is presented. The first phase of the calibration process is broken into three parts: Obtaining reference airspeed, angle of attacks and side slip angles; calibrating MHPs with experimental data; mitigating bias errors to improve calibrations.The method follows the established wind tunnel calibration procedures and includes two additional steps to increase calibration accuracy. The calibration process begins with a computational fluid dynamics (CFD) study on blockage effects in the wind tunnel. CFD results indicate nontrivial deviations of the mean flow due to blockage in wind tunnel test section. Analysis shows a linear relationship between experimental setup position and the resulting deviation from unidirectional flow. The relationship is incorporated into the routine to develop a calibration model. This augments previously demonstrated techniques by processing experimental data from the probe using CFD results. Then the model is refined by removing experimental bias angles.

The next phase is to account for upwash effects caused by the sUAS lifting surfaces. Initial CFD analysis has been conducted to determine the relationship between the perceived airframe orientation measured from the relative wind, and the angle of attack measured by the MHP. Preliminary results show that there is a measurable linear relationship between the perceived and actual angles of attack. The objective these additional steps is to increase the accuracy of MHP calibration and characterize the error in inertial wind vector measured during field experiments.

*Graduate Research Assistant, Smead Aerospace Engineering Sciences, AIAA Member.
†Integrated Remote and In Situ Sensing, Smead Aerospace Engineering Sciences
‡Cooperative Institute for Research in Environmental Sciences, University of Colorado Boulder, Boulder, Colorado, USA, 80309
§Integrated Remote and In Situ Sensing, Smead Aerospace Engineering Sciences
¶Assistant Professor, Smead Aerospace Engineering Sciences
‖Research Scientist (CIRES/NOAA) and Associate Director for Science (IRISS)
**Cooperative Institute for Research in Environmental Sciences, University of Colorado Boulder, Boulder, CO, USA, 80309
††NOAA Physical Sciences Laboratory, Boulder, CO, USA, 80305
‡‡Integrated Remote and In Situ Sensing, University of Colorado, Boulder, CO, USA, 80309
§§Professor, Smead Aerospace Engineering Sciences, AIAA Fellow.
¶¶Assistant Professor, Department of Aerospace and Mechanical Engineering, 500 W University, El Paso, TX 79968, AIAA Member.

I. Nomenclature

α = Angle of Attack
β = Sideslip Angle
γ = Roll Angle
$\tilde{\alpha}$ = Reference Angle of Attack
$\tilde{\beta}$ = Reference Sideslip Angle
q = Reference Dynamic Pressure from Pitot Probe

II. Introduction

Small Uncrewed Aircraft Systems (sUAS) are very flexible platforms and easy to deploy compared to traditional research aircraft. Miniaturization of sensors has made possible complex measurements with sUAS in meteorology or atmospheric science as studying tornadogenesis (ref), tropical clouds (de Boer et al, 2021d), the Arctic boundary layer (de Boer et al, in prep.), or aerosol-cloud interactions (Sanchez et al., 2017). Scientific analysis based on these in situ measurements as turbulence fluxes or cloud entrainment rely on the accuracy of the wind vectors (Thomas et al., 2012, Reineman et al., 2013, Reuder et al. 2012). Multi-hole probes for wind measurements have been used on large aircrafts since the 1960s at the tip of a boom or as radome directly as the nose of the aircraft (Lenshow et al., 1989). Even if calibration of multi-hole probes has been published in the literature decades ago (Treaster and Yocum, 1978; Bohn et al., 1975), its implementation remains difficult, particularly to take into account intrinsic misalignment and bias. Computational fluid dynamics (CFD) becomes complementary to wind tunnel tests to complete accurate MHP calibration and insure better wind vector calculation. MHP measurements are based on differential dynamic pressures and one absolute pressure, which will provide the angle of attack, the angle of sideslip and the airspeed of the aircraft. Standard procedure for calibrating a MHP involves installing the probes in wind tunnels and running the wind tunnel at known air speeds with the probe configured in known angles of attack and side slip. MHPs must be aligned with the incident wind tunnel vector in order to produce the most accurate calibration. Misalignment introduces bias into the calibration and reduces the efficacy of the generated calibration. This study introduces a methodology to determine and correct these biases. Another challenge specifically linked to the section size of the wind tunnel used in the current analysis, is to account for potential blockage effects. Blockage in a wind tunnel will alter an incident wind tunnel vector. Accurate reference values are a requisite to producing an effective calibration. Yet misalignment and blockage are an inevitability especially in small wind tunnels. The motivation of this paper is to augment established calibration techniques by incorporating CFD analysis to account for changes in incident wind tunnel vectors caused by blockage effects.

III. Instrumentation

The first part of the calibration process is conducted numerically via CFD simulation using the Simcenter STAR CCM+ 2020.3.1 CFD package developed by Siemens Digital Industries Software [1]. Extensive use of the wind tunnel is also required for calibration. In order to obtain a large enough data set, the MHP is fixed to a two-stage mount. The first stage enables panning rotation of the setup along the z-axis of the test section and the second stage allows tilting rotation along the x-axis. The pan and tilt combination allows a 15 degree range of motion for both angle of attack and side slip. The rig is placed in the 1-ft $\times$ 1-ft test section. Figure 1a and Figure 1b show the wind tunnel and the MHP setup in the test section.

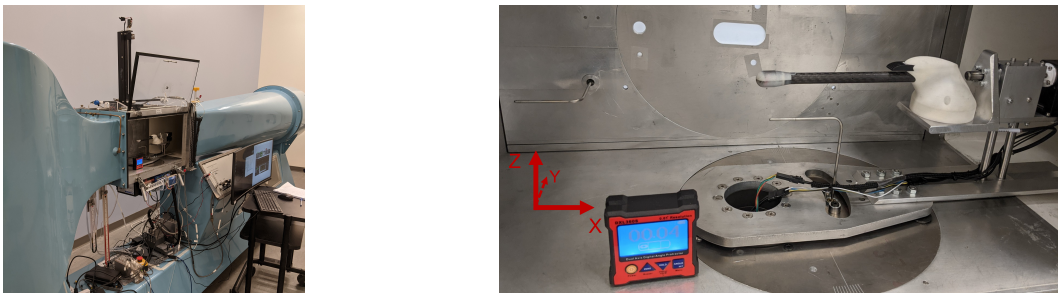

(a) Wind Tunnel **(b) MHP mounted on positioning mechanism**

Fig. 1 Wind Tunnel Setup

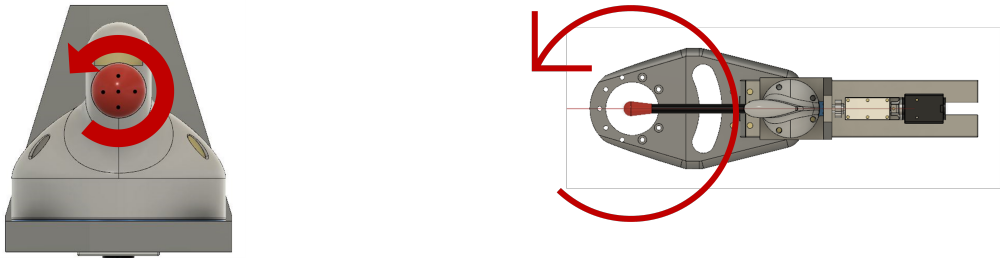

(a) Stage 2: Tilt **(b) Stage 1: Pan**

Fig. 2 Experimental Controls: Pan and Tilt

The calibration is performed on a five-hole MHP. This is the probe that is currently used for the RAAVEN sUAS developed by the University of Colorado's Integrated Remote and In Situ Sensing Progrom (IRISS). The front of the probe contains five ports: one in the center, two along the y-axis, and two along the z-axis. In addition to the five pressure ports located on the probe head; four static pressure ports circumscribe the main boom downstream of the probe head. The configuration is shown in Figure 3.

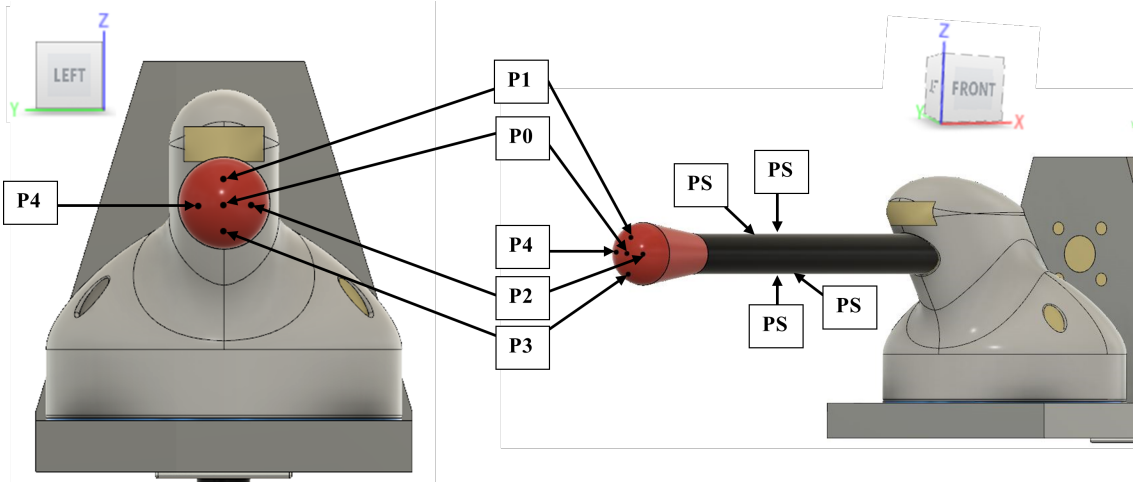

Fig. 3 MHP ports: Five front ports and four hole static ring

The data collected from these ports is used to calculate angle of attack α and sideslip β as well as airspeed. Reference $\tilde{\alpha}$ and $\tilde{\beta}$ determined from pan and tilt positions, and q is determined from the reference pitot probe. Experimental values

are used along with the reference values to calculate non dimensional calibration coefficients.

IV. Measuring Effects of Wind Tunnel Blockage Using CFD

A. Initial Results

CFD simulations were conducted for an empty wind tunnel test section followed by simulations that include the test rig mounted in the test section. Inlet flow conditions were specified as one dimensional uniform flow at the test-section entrance at a speed of 23 ms^{-1} (a typical cruise speed for the RAAVEN sUAS). The selected physics model and mesh criteria are listed in the Tables 4a and 4b.

Models
Three Dimensional
Gas
Segreated Flow
Constant Density
Steady
Turbulent (RANS)
K-ϵ

(a) Selected Physics Models

Meshers	**Values**
Base Size	2 cm
Target Surface Size	75 % Base
Minimum Surface Size	5 % Base
Surface Growth Rate	1.15
Number of Prism Layers	10
Prism Layer Stretching	1.10
Prism Layer Total Thickness	5 % Base
Volume Growth Rate	1.18
Wake Refinement Growth Rate	1.20
Volumetric Control Region Base	50 % Base

(b) Selected Meshers

Fig. 4 Star CCM Physics Models and Mesher Selection

Mesh refinement was conducted in a cylindrical region around the volume of interest near the location of the MHP head. The boom and head of the probe were removed from the model, their contribution the blockage is much less than that of the rest of the rig. Simulations were run for 300 iterations or until residuals had decreased by five decades. After simulations were successfully completed velocity vector components were extracted from the location of the probe head. A range of pan positions were examined using CFD: from 0 to 15 degrees in increments of 2.5 degrees. Figure 5a, Figure 5b and Figure 5c show the cross sectional blockage effects for an empty tunnel; effects for a zeroed setup; and effects for a setup with pan rotated 15 degrees.

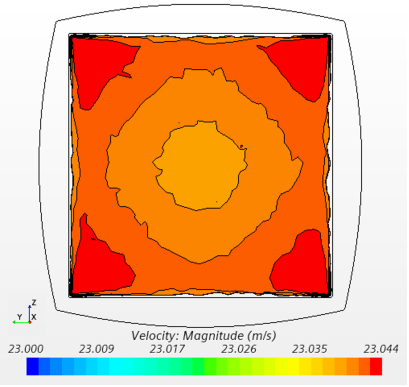

(a) Corner effects in empty wind tunnel simulation

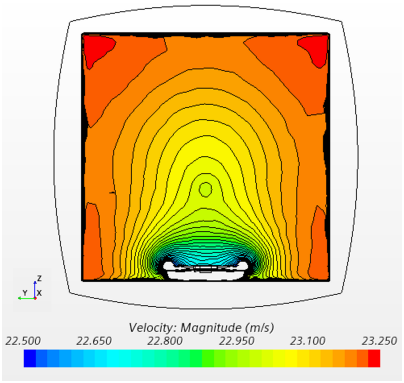

(b) Blockage effects in zeroed experimental setup

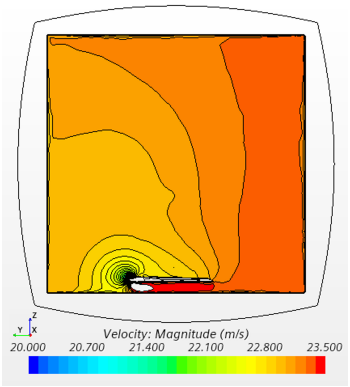

(c) Pan:15 degree blockage effects

Fig. 5 Front view of wind tunnel CFD corner and blockage effects (velocity magnitude) for empty tunnel; with setup in zeroed position; with setup and pan rotated 15 degrees

Figure 5a shows a cross section of the wind tunnel with regions of constant velocity. It is clear the "cleanest" flow is located in the center of the test section. Boundary-layer effects can be seen around the edges particularly in the corners. Figure 5b shows the same cross sections with the addition of the test setup located downstream. The cross section is positioned at the head of the MHP approximately where the pressure ports are located. The presence of obstructions and an incompressibility condition creates flow asymmetries in the vertical direction; however, the flow is symmetric around the z-axis. Figure 5c shows the cross section when pan is set to 15 degrees. Asymmetric flow is observed. Because the blocked area is no longer symmetric, the blockage effects are also asymmetric.

The head of the MHP is located close to center of wind tunnel test section and changes in flow velocity magnitude are shown to be negligible. Further investigation, however, shows that there are significant induced velocities deviating from the inlet velocity direction.

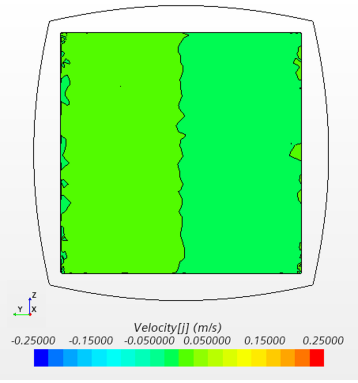

(a) Unidirectional flow in empty wind tunnel

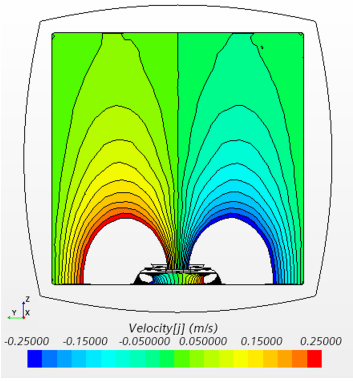

(b) Blockage effects in zeroed experimental setup

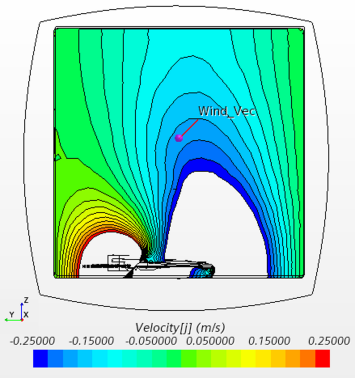

(c) Pan: 15 degree blockage effects

Fig. 6 Front view of wind tunnel CFD corner and blockage effects (j component of velocity) for empty tunnel; with setup in zeroed position; with setup and pan is set to 15 degrees

Figure 6a shows the same cross section as Figure 5a but is a contour plot of flow velocity along the y-axis direction. For an empty tunnel the flow is purely in along the x-axis direction. Figure 6b shows the same cross sections with the addition of the test setup located downstream. A similar result is seen when compared to Figure 5b. With the presence of symmetric obstructions there is a symmetric flow response around the z-axis. Figure 6c shows the cross section when pan is set to 15 degrees. Asymmetric flow is observed. This is challenging to measure experimentally so the results of

these simulations are used to quantify the induced velocities on the incident wind tunnel vector.

The simulation results demonstrate that it is inaccurate to assume that flow at the point of interest is one dimensional or uniform. In fact, the flow field changes as function of stage position. This can be understood when considering the changes in projected area as a function of pan position. An experimental setup with the maximum panning angle projects a larger area onto the wind tunnel cross section than a setup with a zeroed pan angle. Because of incompressibility the air flow speed increases in this region of this cross section. Also, in order to flow past these obstructions, the components of the flow field will change and the velocity field cannot be assumed to be one dimensional.

There is constant offset in the incident wind tunnel vector z component which is not sensitive to stage positions. There is linear relationship between pan positions and incident wind tunnel vector y component. It is surmised that the blockage effects result in a constant induced alpha angle offset and a beta angle offset which is a function of the pan position. The analysis of the CFD simulations are given Table 1, fig. 7a and fig. 7b below.

Pan Angle (degrees)	Induced α Offset (degrees)	Induced β Offset (degrees)
0	0.45	-2.00×10^{-3}
2.5	0.43	-6.80×10^{-2}
5	0.45	-1.77×10^{-1}
7.5	0.42	-2.17×10^{-1}
10	0.44	-3.08×10^{-1}
12.	0.44	-4.04×10^{-1}
15	0.42	-4.81×10^{-1}

Table 1 Determining Relationship between stage position and induced offsets in incident wind tunnel vector

Additional simulations were run to determine if there is a nontrivial effect on the flow when the tilt position is changed. The results of both these experiments are show in Figure 7a and fig. 7b. The figures show that offset effects follow the same trend when tilt position is varied. Therefore, these offsets can be modeled as function of pan position alone.

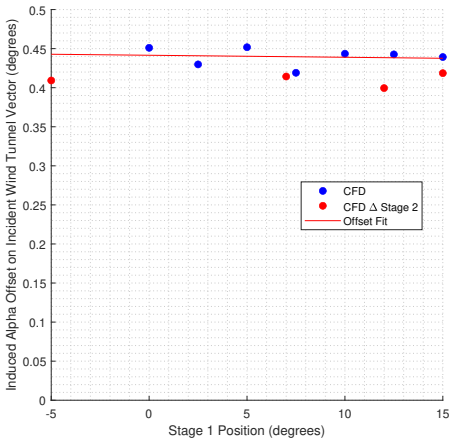

(a) CFD alpha offset

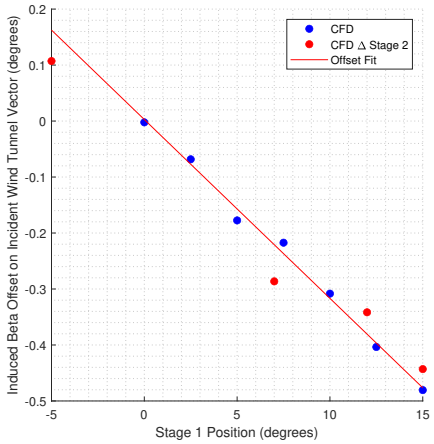

(b) CFD beta offset

Fig. 7 Determining Relationship between stage position and induced offsets in incident wind tunnel vector

The data set created from these simulations were put into function which takes in pan position and returns the corresponding incident wind tunnel vector. This result is then handed to another calibration function which uses the incident wind vector, pan and tilt positions to compute reference $\tilde{\alpha}$ and $\tilde{\beta}$ values. These are the values that are used for computing calibration coefficients.

V. Probe Calibration

A. Wind Tunnel Setup

1. Selecting Wind Tunnel Parameters

There is extensive information published on calibrating MHPs with wind tunnels. Several previously published journal articles have shown that reasonable speeds to run the wind tunnel range between 15 and 25 ms^{-1} at and reasonable α and β angles lie between -15 and 15 degrees [2][3]. This is also tenable with the equipment used for this project. The wind tunnel was run at roughly 23 ms^{-1} and the experimental apparatus was designed to sweep a range of -15 to 15 degrees for α and β angles.

2. Reference Frames: From Wind Tunnel to Probe

The wind tunnel set up is a two-stage rig. The MHP is commanded Various combinations of pan and tilt positions to simulate realistic α and β angles that would be experienced during flight. To change between the Wind tunnel reference frame and the MHP reference frame there are two transformations and three frames:

1) Wind Tunnel Reference Frame
2) Pan Angle
3) Tilt Angle

Where the pan and tilt angles are the specified system rotations and corresponding transformations are applied to the wind tunnel vector. The final tilt transformation outputs the wind vector in the MHP reference frame.

$$^{MHP}v = (^{MHP}R_{S2})(^{S2}R_{S1})(^{S1}R_{WT})(^{WT}v) \tag{1}$$

Here ^{MHP}v is the incident wind vector in the multi-hole probe reference frame; S2 refers to tilt; S1 is pan; and WT is the wind tunnel reference frame. For this setup the reference frame transformations are purely rotations. The general form for a rotation matrix with Euler angles ϕ, θ and ψ is given by:

$$^{WT}v = \begin{bmatrix} u \\ v \\ w \end{bmatrix} \qquad \tilde{\alpha} = \tan^{-1}\left(\frac{w}{u}\right) \qquad \tilde{\beta} = \tan^{-1}\left(\frac{v}{u}\right) \tag{2}$$

These $\tilde{\alpha}$ and $\tilde{\beta}$ reference values are used in the calibration process to determine calibration coefficients for the MHP.

B. Finding Calibration Coefficients

Extensive work has already been done to develop calibration routines from wind tunnel data. The MHP used has five non-connected ports on the head of the probe. Techniques outlined in papers by Kroonenberg et. al. [4], Wildmann et. al. [3] and Calmer et al. [2] are applied.

Five pressure differentials are calculated using the front five pressure ports on the MHP. The first values that are calculated are the differences between the off-center ports with the center port. The next value that is computed is a total pressure difference value. Then, nondimensional pressure coefficients k_α and k_β are determined. These nondimensional values are well defined by previous publications and this is a standard technique to use for calibrating an MHP.

Variable	dP_i(Pa)	Δ P (Pa)	k_α	k_β	k_q
Equation	$P_i - P_S$	$\frac{1}{4}\sum_{i=1}^{4} dP_i$	$\frac{dP_1 - dP_3}{\Delta P}$	$\frac{dP_2 - dP_4}{\Delta P}$	$\frac{q - dP_0}{dP_0 - \Delta P}$

Table 2 Calibration Variables: From Wildmann et. al. [3]

1. Computing α and β and airspeed Calibration Coefficients

The values of α and β are modeled as functions of k_α and k_β. Values of m and n set the order for k_α and k_β polynomial matrices. For this experiment $m = n = 2$ was chosen to avoid over fitting data and to match the expected even behavior of the function.

$$f_{\alpha,\beta,k_q}(k_\alpha, k_\beta) = \sum_{i=0}^{m} k_\alpha^i \sum_{j=0}^{n} X_{ij} k_\beta^j \tag{3}$$

This can be written in matrix form:

$$\alpha, \beta, k_q = \begin{bmatrix} k_\alpha^n & k_\alpha^{n-1} & \dots & k_\alpha^0 \end{bmatrix} \begin{bmatrix} X \end{bmatrix} \begin{bmatrix} k_\beta^m \\ k_\beta^{m-1} \\ \vdots \\ k_\beta^0 \end{bmatrix} \tag{4}$$

A calibration coefficient matrix X is computed for α and β. In order to determine X reference values $\tilde{\alpha}$ and $\tilde{\beta}$ are used from the wind tunnel routine. To simplify the process of solving for X, the problem can be taken to one dimension, converted to a linear least-squares problem.

$$\tilde{\alpha} = \sum_{i=0}^{n} \sum_{j=0}^{m} k_\alpha^i k_\beta^j X_{i\times(j-1)+j+1} \tag{5}$$

$$\tilde{\alpha} = \begin{bmatrix} k_\alpha^0 k_\beta^0 & k_\alpha^0 k_\beta^1 & \dots & k_\alpha^0 k_\beta^m & k_\alpha^1 k_\beta^0 & k_\alpha^1 k_\beta^1 & \dots & k_\alpha^n k_\beta^m \end{bmatrix} \begin{bmatrix} X \end{bmatrix} = K_{\alpha\beta} X \tag{6}$$

$$X_\alpha = (K_{\alpha\beta}^T K_{\alpha\beta})^{-1} K_{\alpha\beta}^T \tilde{\alpha} \tag{7}$$

The calibration coefficients, X_β are computed in the same way X_α coefficients are, using $\tilde{\beta}$ instead of $\tilde{\alpha}$. For this method of calibration each X is a column vector of length $(m + 1) \times (n + 1)$. If the calibration is sufficiently accurate, they can be used to process raw data from field campaigns to estimate α and β angles.

At this point the process diverges slightly for calibrating air speed. The value for airspeed is modeled as function of k_q. Since k_q is a value that can be computed using the dynamic pressure q from the reference pitot tube:

$$k_q = \frac{dP_0 - q}{dP_0 - \Delta P} \tag{8}$$

The rest of the calibration process follows the same routine:

$$X_{k_q} = (K_{\alpha\beta}^T K_{\alpha\beta})^{-1} K_{\alpha\beta}^T k_q \tag{9}$$

2. Evaluating Calibration

Figure 8a and Figure 8b show the results of a wind tunnel calibration trial. In Figure 8a the green points represent $\tilde{\alpha}$ and $\tilde{\beta}$ values and the magenta points represent the calibrated experimental values from the MHP. In Figure 8b the red points represent the reference airspeed and blue points represent calibrated experimental values from the MHP.

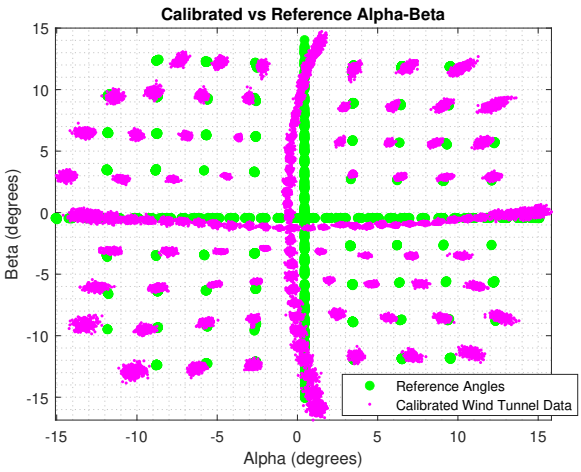

(a) First Calibration: Alpha-Beta

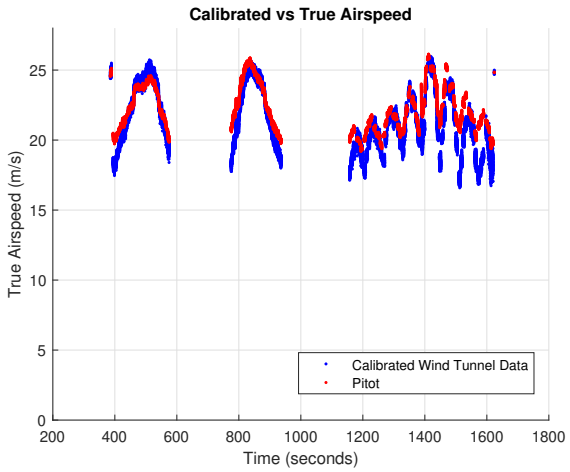

(b) First Calibration: Airspeed

Fig. 8 Determining relationship between stage position and induced offsets in incident wind tunnel vector

When the calibration is applied to the wind tunnel data, the computed airspeed closely and sufficiently follows the reference airspeed. However, the calibration for α and β angles needs improvement. When the calibration is applied to data the fitted data appears to be warped. A possible reason is that reference the reference $\tilde{\alpha}$ and $\tilde{\beta}$ are inaccurate. Errors in $\tilde{\alpha}$ and $\tilde{\beta}$ can be attributed to angle biases which arise when mounting the rig and MHP into the wind tunnel.

VI. Accounting For Angle Bias in Experimental Setup

1. Reference Frames: From Wind Tunnel to Probe

Biases are introduced when the experimental setup is assembled and places into the wind tunnel. There are three places where bias angles can occur:

1) Between the wind tunnel and the first stage
2) Between the first stage and second stage
3) Between the second stage and the MHP

An inclinometer was used to estimate the biases in the wind tunnel setup. The process of finding the MHP reference frame from the wind tunnel reference frame is now broken into five transformations and six frames:

1) Wind Tunnel Reference Frame
2) Pan Bias
3) Pan Angle
4) Tilt Bias
5) Tilt Angle
6) MHP

Where the pan and tilt angles are the specified system rotations and biases are results of imperfections in the machining and construction of the stages. The biases are measured when pan and tilt are set to zero and are found using an inclinometer. The bias angles are determined only for the non-rotating axes of each stage and are recorded as Euler angles. Once this information is determined the five corresponding transformations are applied to the wind tunnel vector. This outputs the wind vector in the MHP reference frame.

$$^{MHP}v = (^{MHP}R_{S2})(^{S2}R_{S2B})(^{S2B}R_{S1})(^{S1}R_{S1B})(^{S1B}R_{WT})(^{WT}v) \tag{10}$$

Where MHP is the multi-hole probe reference frame; S2 is tilt; S2B is the tilt bias; S1 is pan; S1B is pan bias; and WT is the wind tunnel reference frame.

The method of removing angle biases can be challenging. Attempting to measure biases introduces additional coordinate systems which likely contain error themselves [5]. Error can be mitigated by estimating angle biases with computational methods.To remove the biases an optimization code was used. The calibration was used in a grid search to find the set of bias angles which minimized L2 norm error (including error from reference $\tilde{\alpha}$ and $\tilde{\beta}$ angles) and calibrated results. As stated previously, measurements were made with an inclinometer to determine which angles to test and what point to search around. The biases found are listed in Table 3.

Euler Angle	Stage 1 Bias (degrees)	Stage 2 Bias (degrees)	MHP Mounting Bias (degrees)
ϕ	2.0	0	0
θ	0	0.5	0
ψ	0	0	0

Table 3 Optimized Installation Stage Biases

After applying these biases to the calibration routine the reference $\tilde{\alpha}$ and $\tilde{\beta}$ are improved and more accurately reflect the experimental setup. The newly calibrated coefficients are improved and are better aligned with the reference data. This can be seen in Figure 9b below.

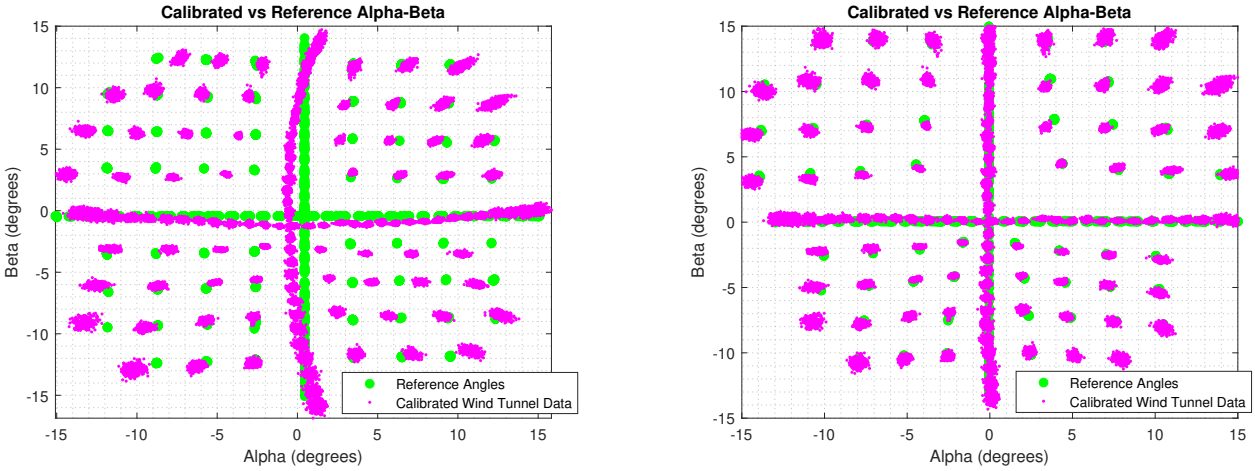

(a) Biased Calibration **(b) Unbiased Calibration**

Fig. 9 Comparing Calibrations: Experimental setup angular bias removal

VII. Conclusions

The results of CFD simulations confirmed the existence of small but non-trivial blockage effects near the MHP head. This was unsurprising due to the small size of the wind tunnel cross section and relatively large size of the experimental rig. As a result of the blockage there is a constant offset in α and an offset in β that is a linear function of pan position.

These CFD results were used to augment established MHP calibration procedures. Then an optimization routine was run to remove biases related to setup and installation of the experimental apparatus in the wind tunnel test section. An inclinometer was used to measure biases in each of the main reference frames – these measurements were used as a starting point for the optimization routine. After all steps of the calibration routine were performed sets of calibration coefficients were produced.

There are further potential areas were CFD might be used to improve wind vector measurements from sUASs. An

investigation of airframe effects on angle of attack has been started. Initial results have shown a measurable relationship between α,β and the induced offsets in α and β a the location of the MHP head. The initial results are discussed in the following section.

VIII. Further Discussion: Accounting for Airframe Effects

The next step of MHP calibration is determining the upwash effects on the wind vector at the probe location. The RAAVEN has a blended wing-body fuselage with an airfoil-shaped longitudinal cross section. The combined wing-body lifting-surface produces an upwash upstream of the airframe nose. Figure 10 shows a cross section along the center line of the RAAVEN at small angle of attack. The air upstream of the nose is clearly affected by the airframe.

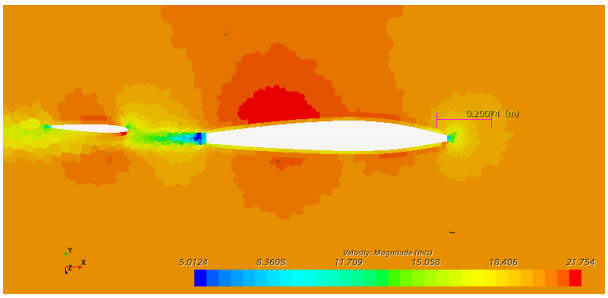

Fig. 10 Up-wash Effect in Front of RAAVEN Airframe

The MHP pressure ports do not extend beyond this region and designing a probe with a longer boom would introduce other issues. As such a CFD investigation was conducted to determine if upwash effects can be accounted for and included in a calibration routine.

1. Varied α

CFD simulations were designed with varying α and β values to determine if it is possible to account for upwash effects. In the simulations, α and β angles were specified, and a probe point was placed at location of the MPH ports. Using the wind vector components perceived α was extracted at the probe point and was plotted against the input α values. This was done for a range of input α and wind speed values. The results of these simulations are plotted in Figure 11.

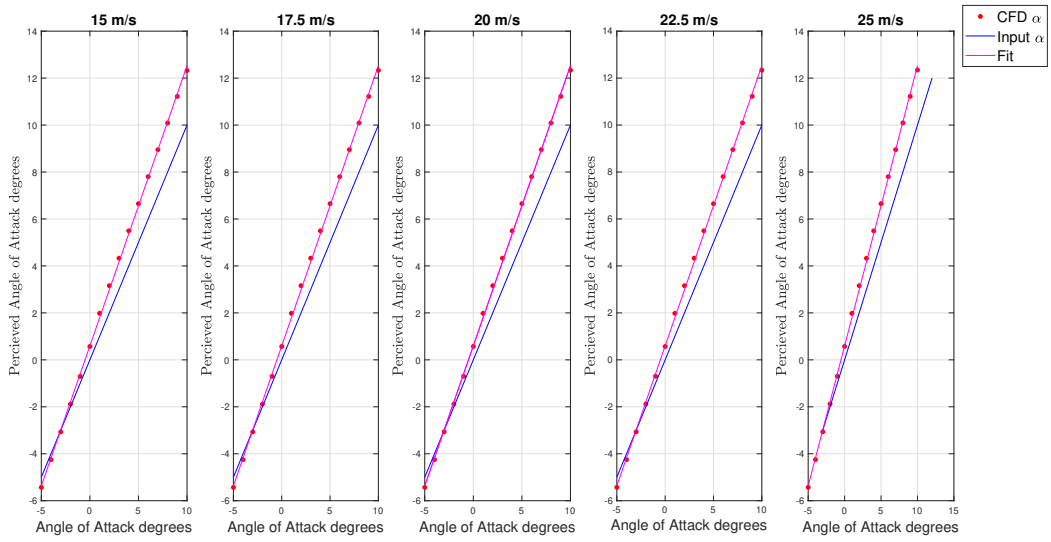

Fig. 11 Up-wash Effect on Angle of Attack Measurement for Varied Speeds

Speed (ms^{-1})	Slope	Intercept
15	1.19	5.95×10^{-1}
17.5	1.19	5.94×10^{-1}
20	1.19	5.96×10^{-1}
22.5	1.19	5.96×10^{-1}
25	1.19	5.96×10^{-1}

Table 4 Up-wash Effect on Angle of Attack Measurement for Varied Speeds: Regression Fit

Figure 11 and Table 4 reveal that the upwash effect is increased as α is increased and that the relationship is not dependent on wind speed. They also show that the relationship is linear. Therefore, the initial results from these simulations indicate that will be possible to account for upwash effects on the probe.

2. Varied β

The similar simulations were then conducted to evaluate the airframe influence on perceived β values at the probe location. Again, the simulations were run for varied β and wind speed values.

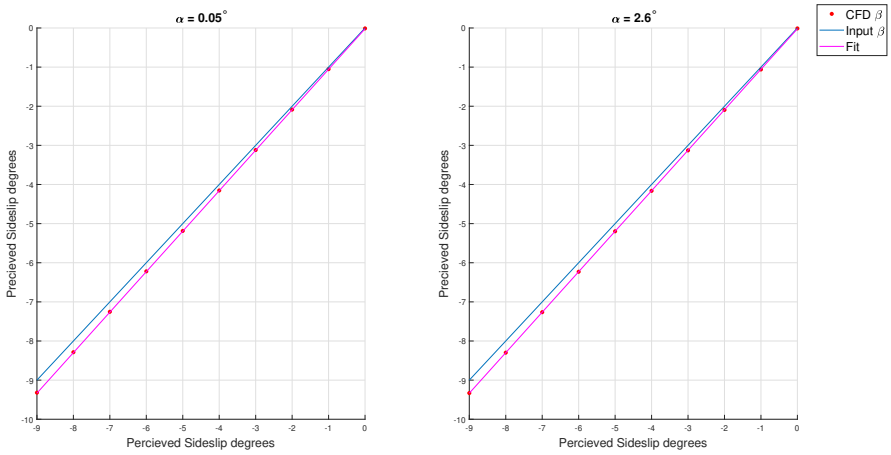

Fig. 12 Airframe Effect on β Angle Measurement at 17.5 $\mathrm{m\,s^{-1}}$

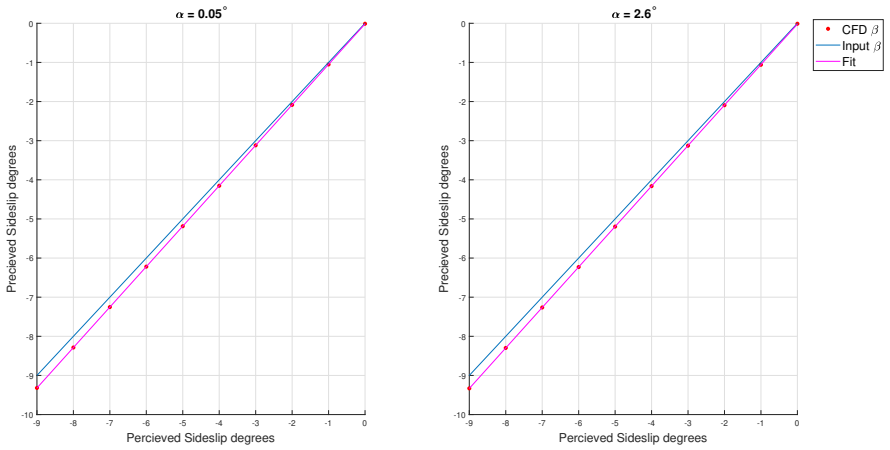

Fig. 13 Airframe Effect on β Angle Measurement at 25 $\mathrm{m\,s^{-1}}$

Speed (m $\mathrm{m\,s^{-1}}$**)**	**Angle of Attack (α°)**	**Slope**	**Intercept**
17.5	0.05	1.03	-1.60×10^{-2}
17.5	2.6	1.03	-2.12×10^{-2}
25	0.05	1.03	-1.59×10^{-2}
25	2.6	1.03	-2.12×10^{-1}

Table 5 Up-wash Effect on Angle of Attack Measurement for Varied Speeds: Regression Fit

Figures 12 and 13 and Table 4 show the results of these simulations. In this case the results indicate that the airframe has a much smaller impact on the perceived value of β. The results do not appear to be sensitive to varied wind speed or to varied α or β values. However, there does appear to be small differences between perceived β and input β with a linear correlation. Though the two values are almost equal, this linear relation can be used to improve the MHP calibration.

3. Comments on Current Results/Next Steps

Preliminary results from these simulations are positive. Attempting to account for upwash effects on the MHP measurements appears to be a tenable goal. The next step is to conduct more simulations to account for recent changes in probe design.

IX. Verification of CFD Models

A convergence study was conducted to validate confidence in the CFD models used for this calibration process. The study examined the effect of the computational cell growth rate in the unstructured grid on the results. These simulations modeled both empty wind tunnel test section and a wind tunnel test section with the MHP calibration setup.

A. Cell Growth Rate

Again, for each of the simulations residuals for turbulence kinetic energy, turbulence dissipation rate, continuity, and X-Y-Z momentum values all decay to values below 10^{-5}. This gives confidence that the model is asymptotically converging.

Cell Growth Rate	Probe Static Pressure (Pa)	Probe 1 U (ms^{-1})	Probe 1 V (ms^{-1})	Probe 1 W (ms^{-1})
1.18	11.91	17.87	0.76	0.00
1.31	11.91	17.87	0.00	0.00
1.46	12.11	17.87	0.00	0.00
1.62	12.00	17.87	0.00	0.00
1.80	12.00	17.87	0.00	0.00
2.00	12.19	17.87	0.00	0.00

Table 6 Cell Growth Rate Effect on Convergence for Full Wind Tunnel Simulation

Cell Growth Rate	Probe Static Pressure (Pa)	Probe 1 U (ms^{-1})	Probe 1 V (ms^{-1})	Probe 1 W (ms^{-1})
1.18	93.51	3.35	0.76	2.25
1.31	94.02	2.31	0.80	1.91
1.46	94.01	2.33	0.82	1.84
1.62	91.23	8.43	1.09	3.82
1.80	88.93	5.60	1.06	3.06
2.00	89.83	8.01	1.14	3.63

Table 7 Cell Growth Rate Effect on Convergence for Full Wind Tunnel Simulation

Tables 6 and 7 offer validation for these CFD simulations because the results at the probe point are consistent enough to create confidence in the solutions. The fact that residuals were reduced by five orders of magnitude creates additional confidence in the simulation solutions.

Acknowledgments

This material is based upon work supported by the National Science Foundation under Grand No. AGS 1824609 and by the National Science Foundation Graduate Research Fellowship under Grant No. DGE 2040434.

References

[1] Siemens Digital Industries Software, "Simcenter STAR-CCM+, version 2020.3.1," , Siemens 2020.

[2] Calmer, R., Roberts, G. C., Preissler, J., Sanchez, K. J., Derrien, S., and O'Dowd, C., "Vertical wind velocity measurements using a five-hole probe with remotely piloted aircraft to study aerosol–cloud interactions," *Atmospheric Measurement Techniques*,

Vol. 11, No. 5, 2018, pp. 2583–2599. https://doi.org/10.5194/amt-11-2583-2018, URL https://amt.copernicus.org/articles/11/2583/2018/.

[3] Wildmann, N. R., and Bange, J., "Towards high accuracy and better frequency response with standard multi-hole probes in turbulence measurement with remotely piloted aircraft (RP," *Atmoshperic Measurment Techniques*, 2014, p. 1031.

[4] van den Kroonenberg, A., Martin, T., and coauthors, "Measuring the Wind Vector Using the Autonomous Mini Aerial Vehicle M^2AV," *American Meteorological Society*, 2008, $pp.1971 - -1973$.

[5] Zeiger, M., and Schaeffler, N., "Correcting multi-hole probe alignment bias errors post-calibration," 2001. https://doi.org/10.2514/6.2001-900.

[6] de Boer, G., Borenstein, S., Calmer, R., Cox, C., Rhodes, M., Choate, C., Hamilton, J., Osborn, J., Lawrence, D., Argrow, B., and Intrieri, J., "Measurements from the University of Colorado RAAVEN Uncrewed Aircraft System during ATOMIC," *Earth System Science Data Discussions*, Vol. 2021, 2021, pp. 1–22. https://doi.org/10.5194/essd-2021-175, URL https://essd.copernicus.org/preprints/essd-2021-175/.

[7] de Boer, G., Calmer, R., Jozef, G., Cassano, J., Hamilton, J., Lawrence, D., Borenstein, S., Doddi, A., Cox, C., Schmale, J., Preußer, A., and Argrow, B., "Observing the Central Arctic Atmosphere and Surface with University of Colorado Uncrewed Aircraft Systems," *Nature Sci. Data*, in Prep.

[8] Lenschow, D., and P., S.-D., "Measurement Techniques: Air Motion Sensing," *RAF Bulletin 23:National Center for Atmospheric Research*, 1989. URL https://www.eol.ucar.edu/content/raf-bulletin-no-23.

[9] Sankaralingam, L., and Ramprasadh, C., "Angle of attack measurement using low-cost 3D printed five hole probe for UAV applications," *Measurement*, Vol. 168, 2021, p. 108379. https://doi.org/https://doi.org/10.1016/j.measurement.2020.108379, URL https://www.sciencedirect.com/science/article/pii/S0263224120309155.

[10] Ross, A. L., Jacob, J. D., and Arena, A. S., *Continued Design and Development of a Tornado Intercept Unmanned Aerial Vehicle*, 2020. https://doi.org/10.2514/6.2020-2629, URL https://arc.aiaa.org/doi/abs/10.2514/6.2020-2629.

[11] Noca, F., Catry, G., Bosson, N., Bardazzi, L., Marquez, S., and Gros, A., "Wind and Weather Facility for Testing Free-Flying Drones," 2019. https://doi.org/10.2514/6.2019-2861.

[12] Pang, B., Ng, E. M., and Low, K. H., *UAV Trajectory Estimation and Deviation Analysis for Contingency Management in Urban Environments*, 2020. https://doi.org/10.2514/6.2020-2919, URL https://arc.aiaa.org/doi/abs/10.2514/6.2020-2919.

[13] Reineman, B. D., Lenain, L., Statom, N. M., and Melville, W. K., "Development and Testing of Instrumentation for UAV-Based Flux Measurements within Terrestrial and Marine Atmospheric Boundary Layers," *Journal of Atmospheric and Oceanic Technology*, Vol. 30, No. 7, 2013, pp. 1295–1319. https://doi.org/10.1175/jtech-d-12-00176.1.

[14] Reuder, J., Båserud, L., Jonassen, M. O., Kral, S. T., and Müller, M., "Exploring the potential of the RPA system SUMO for multipurpose boundary-layer missions during the BLLAST campaign," *Atmospheric Measurement Techniques*, Vol. 9, No. 6, 2016, pp. 2675–2688. https://doi.org/10.5194/amt-9-2675-2016.

[15] Sanchez, K. J., Roberts, G. C., Calmer, R., Nicoll, K., Hashimshoni, E., Rosenfeld, D., Ovadnevaite, J., Preissler, J., Ceburnis, D., O'Dowd, C., and Russell, L. M., "Top-down and bottom-up aerosol–cloud closure: towards understanding sources of uncertainty in deriving cloud shortwave radiative flux," *Atmospheric Chemistry and Physics*, Vol. 17, No. 16, 2017, pp. 9797–9814. https://doi.org/10.5194/acp-17-9797-2017.

[16] Thomas, R. M., Lehmann, K., Nguyen, H., Jackson, D. L., Wolfe, D., and Ramanathan, V., "Measurement of turbulent water vapor fluxes using a lightweight unmanned aerial vehicle system," *Atmospheric Measurement Techniques*, Vol. 5, No. 1, 2012, pp. 243–257. https://doi.org/10.5194/amt-5-243-2012.

[17] Treaster, A. L., and Yocum, A. M., "The calibration and application of five-hole probes," *24th International Instrumentation Symposium*, 1978, pp. 255–266.